



The Orbit of WASP-12b Is Decaying

Samuel W. Yee¹, Joshua N. Winn¹, Heather A. Knutson², Kishore C. Patra³, Shreyas Vissapragada²,
Michael M. Zhang², Matthew J. Holman⁴, Avi Shporer⁵, and Jason T. Wright^{6,7}

¹ Department of Astrophysical Sciences, Princeton University, 4 Ivy Lane, Princeton, NJ 08540, USA; swyee@princeton.edu

² Division of Geological and Planetary Sciences, California Institute of Technology, 1200 California Boulevard, Pasadena, CA 91125, USA

³ Department of Astronomy, University of California, Berkeley, CA 94720, USA

⁴ Harvard-Smithsonian Center for Astrophysics, 60 Garden Street, Cambridge, MA 02138, USA

⁵ Department of Physics and Kavli Institute for Astrophysics and Space Research, Massachusetts Institute of Technology, Cambridge, MA 02139, USA

⁶ Department of Astronomy & Astrophysics, 525 Davey Laboratory, The Pennsylvania State University, University Park, PA, 16802, USA

⁷ Center for Exoplanets and Habitable Worlds, 525 Davey Laboratory, The Pennsylvania State University, University Park, PA, 16802, USA

Received 2019 September 30; revised 2019 November 14; accepted 2019 November 19; published 2019 December 27

Abstract

WASP-12b is a transiting hot Jupiter on a 1.09 day orbit around a late-F star. Since the planet's discovery in 2008, the time interval between transits has been decreasing by 29 ± 2 ms yr⁻¹. This is a possible sign of orbital decay, although the previously available data left open the possibility that the planet's orbit is slightly eccentric and is undergoing apsidal precession. Here, we present new transit and occultation observations that provide more decisive evidence for orbital decay, which is favored over apsidal precession by a Δ BIC of 22.3 or Bayes factor of 70,000. We also present new radial-velocity data that rule out the Rømer effect as the cause of the period change. This makes WASP-12 the first planetary system for which we can be confident that the orbit is decaying. The decay timescale for the orbit is $P/\dot{P} = 3.25 \pm 0.23$ Myr. Interpreting the decay as the result of tidal dissipation, the modified stellar tidal quality factor is $Q'_* = 1.8 \times 10^5$.

Unified Astronomy Thesaurus concepts: Hot Jupiters (753); Exoplanets (498); Transit photometry (1709)

Supporting material: machine-readable tables

1. Introduction

There are several reasons why the orbital period of a hot Jupiter might change, or appear to change. Interactions with other planets cause transit-timing variations, although it is now well established that hot Jupiters tend to lack planetary companions close enough or massive enough to produce detectable variations (see, e.g., Steffen et al. 2012; Huang et al. 2016). On secular timescales, a planetary or stellar companion can induce orbital precession (Miralda-Escudé 2002) or Kozai–Lidov cycles (Holman et al. 1997; Innanen et al. 1997; Mazeh et al. 1997). Even in the absence of external perturbers, an eccentric orbit will precess due to general relativity and the quadrupole fields from rotational and tidal bulges (Jordán & Bakos 2008; Pál & Kocsis 2008). There are also the long-term effects of tidal dissipation, which for hot Jupiters are expected to lead to orbital circularization, coplanarization, and decay (Counselman 1973; Hut 1980; Rasio et al. 1996; Levrard et al. 2009). Mass loss might cause the orbit to expand or contract, depending on the specific angular momentum of the escaping material and where it is ultimately deposited (see, e.g., Valsecchi et al. 2015; Jackson et al. 2016). Finally, any long-term acceleration of the host star will cause an illusory change in period due to the associated changes in the light-travel time, known as the Rømer effect. Such an acceleration would likely be due to a wide-orbiting companion.

Of all these possibilities, the most interesting are probably tidal orbital decay, mass loss, and apsidal precession, because the measured rate of change would give us insight into a poorly understood phenomenon. The rate of tidal orbital decay depends on the unknown mechanisms by which the stellar tidal oscillations are dissipated as heat (Rasio et al. 1996; Sasselov 2003). Mass loss could be due to an escaping wind, or Roche lobe overflow, either of which could be precipitated by tidal orbital decay (Valsecchi et al. 2015). The rate of apsidal

precession is expected to be dominated by the contribution from the planet's tidal deformability, and therefore, the measured rate would give us a glimpse into the planet's interior structure (Ragozzine & Wolf 2009).

Currently, the most promising system for observing these effects is WASP-12 (Hebb et al. 2009; Haswell 2018). The host star is a late-F star ($T_{\text{eff}} \approx 6300$ K; Hebb et al. 2009). The planet is a hot Jupiter with orbital period 1.09 days, mass $1.47 M_J$, and radius $1.90 R_J$ (Collins et al. 2017). This radius is unusually large even by the standards of hot Jupiters, and ultraviolet transit observations imply an even larger cloud of diffuse gas, indicating that the planet has an escaping exosphere (Li et al. 2010; Fossati et al. 2010; Haswell et al. 2012; Nichols et al. 2015). Furthermore, there is evidence for variations in the time interval between transits. Maciejewski et al. (2011) reported the detection of short-timescale variations, although subsequent analysis by Maciejewski et al. (2013) showed that the statistical significance was weaker than originally reported. Maciejewski et al. (2013) also presented a larger database of transit times and found evidence that the interval between transits is varying sinusoidally with a 500 day period. They hypothesized that the anomalies were due to a second planet in the system with a mass of $0.1 M_J$ and a period of 3.5 days.

After accumulating more data, Maciejewski et al. (2016) did not confirm the sinusoidal variability, but instead found a quadratic trend consistent with a uniformly decreasing orbital period. Patra et al. (2017) presented new data and confirmed that the observed interval between transits has been decreasing, at a rate of 29 ± 3 ms yr⁻¹. Patra et al. (2017) also showed that the available radial-velocity data were incompatible with a line-of-sight acceleration large enough for the Rømer effect to be the sole explanation for the apparent decrease in orbital period. Additional transit times have since been reported by Maciejewski et al. (2018)

and Baluev et al. (2019), in both cases supporting the finding of a long-term decrease in the transit period.

Bailey & Goodman (2019) considered and discarded many explanations for the period decrease besides tidal orbital decay, such as the Applegate effect or gravitational perturbations from another planet. However, the possibility remained that the orbit is eccentric and apsidally precessing, and that the apparently quadratic trend in the transit timing deviations is really a portion of a long-period sinusoidal pattern. The radial-velocity data rule out eccentricities larger than about 0.03, but even an eccentricity on the order of 10^{-3} would be sufficient to fit the data under this hypothesis.

One way to tell the difference between orbital decay and apsidal precession is to measure the times of occultations (secondary eclipses). In the case of orbital decay, the time interval between occultations would be shrinking at the same rate as the time interval between transits. In contrast, for a precessing orbit, the transit and occultation timing deviations would have opposite signs. Patra et al. (2017) analyzed all of the available occultation times and found that both models gave a reasonable fit to the data. They found a preference for orbital decay over apsidal precession, but because the statistical significance was modest ($\Delta\chi^2 = 5.5$), they stopped short of claiming conclusive evidence for orbital decay. By extrapolating both models into the future, Patra et al. (2017) showed that observations of occultations over the next few years would allow for a more definitive conclusion.

Two years have now elapsed. In this paper, we report new observations of transits (Section 2) and occultations (Section 3), as well as additional radial-velocity data (Section 4). We present an analysis of all the available data, finding that orbital decay is favored over apsidal precession with greater confidence than before (Section 5). Finally, we discuss the possible implications of the observed decay rate for our understanding of hot Jupiters and stellar interiors (Section 6).

2. New Transit Observations

We observed 10 transits of WASP-12b with the 1.2m telescope at the Fred Lawrence Whipple Observatory (FLWO) on Mt. Hopkins, Arizona, between 2017 November and 2019 January. The observations were made with *Keplercam* and a Sloan r' -band filter, with an exposure time of 15 s, yielding a typical signal-to-noise ratio of 200 per frame. We reduced the data with standard procedures, as described by Patra et al. (2017). We performed circular-aperture photometry of WASP-12 and 7–9 comparison stars. The aperture radius was typically 7–8 pixels, chosen to minimize the scatter in the out-of-transit flux of WASP-12 relative to the comparison stars. We then produced light curves by dividing the flux of WASP-12 by the sum of the comparison star fluxes, and then normalizing to set the median flux equal to unity outside of the transits. The estimated uncertainty in each data point was taken to be the standard deviation of the flux time series outside of transits. The photometric time series is provided in Table 1.

To measure transit times, we fitted a standard transit model (Mandel & Agol 2002). We assumed a quadratic limb-darkening law with coefficients $u_1 = 0.32$, $u_2 = 0.32$, as tabulated by Claret & Bloemen (2011) for a star having the spectroscopic properties $T_{\text{eff}} = 6290$ K, $[\text{Fe}/\text{H}] = 0.3$, $\log g = 4.3$ (Hebb et al. 2009).⁸

⁸ Here, we used the online tool of Eastman et al. (2013) at <http://astroutils.astronomy.ohio-state.edu/exofast/limbdark.shtml> to interpolate the Claret & Bloemen (2011) tables.

Table 1
Photometric Timeseries

BJD _{TDB}	Normalized Flux	$\sigma(\text{Flux})$	Code ^a
2458123.68083	0.9980	0.0014	F1666
2458123.68118	0.9985	0.0014	F1666
2458123.68153	0.9991	0.0014	F1666
2458123.68192	1.0000	0.0014	F1666
2458123.68233	0.9992	0.0014	F1666
2458123.68270	1.0000	0.0014	F1666
2458123.68305	0.9997	0.0014	F1666
2458123.68340	0.9993	0.0014	F1666

Note.

^a Code denotes the source and orbit number for each data point. The first character represents the source telescope—F for FLWO transit observations, S for *Spitzer* occultation observations, and W for WIRC occultation observations.

(This table is available in its entirety in machine-readable form.)

We obtained the best fit to each light curve by minimizing the usual χ^2 statistic. We then used the *emcee* code (Goodman & Weare 2010; Foreman-Mackey et al. 2013) to perform an affine-invariant Markov Chain Monte Carlo (MCMC) sampling to determine the uncertainties in the model parameters, including the transit time (the midpoint of the transit, or the time of minimum light). We discarded the first $\sim 30\%$ of the MCMC chains as burn-in, and ensured convergence by comparing chains from multiple MCMC runs with the Gelman–Rubin statistic (Gelman & Rubin 1992). Figure 1 shows the new light curves and the best-fitting model curves. Table 5 gives the transit times and uncertainties. The typical uncertainty is 30 s, comparable to the precision obtained by Patra et al. (2017).

3. New Occultation Observations

3.1. *Spitzer* Occultations

We observed four occultations of WASP-12b with the *Spitzer Space Telescope* in 2019 January and February. The first and last event were separated by 16 planetary orbits. All of the data were obtained with the $4.5\ \mu\text{m}$ channel, in 32×32 pixel subarray mode with 2 s exposures. For each event, approximately 11,000 exposures were obtained over a timespan of 7 hr bracketing the 3 hr duration of the occultation.

To reduce the data, we first determined the background level in each exposure by calculating the median flux in the image after excluding the pixels associated with the host star. We subtracted this background level from each image. Then, to measure the pixel location of the centroid of the stellar image, we fitted a two-dimensional Gaussian function to the central 25 pixels of each exposure. Using these centroid positions, we performed circular-aperture photometry, with trial aperture radii ranging from 1.6 to 3.5 pixels in 0.1 pixel increments. We identified a few outliers based on an unusually large deviation in the centroid time series; specifically, we flagged any exposures for which the centroid coordinates were more than 5σ away from the median of the surrounding 10 exposures. The flux values for the offending exposures were replaced by the median flux value within that same 10-exposure window. We also removed from consideration a few data points from the orbit 2026 data set that had obvious image artifacts.

To correct for the well-known effects of intra-pixel sensitivity variations, we used the Pixel Level Decorrelation

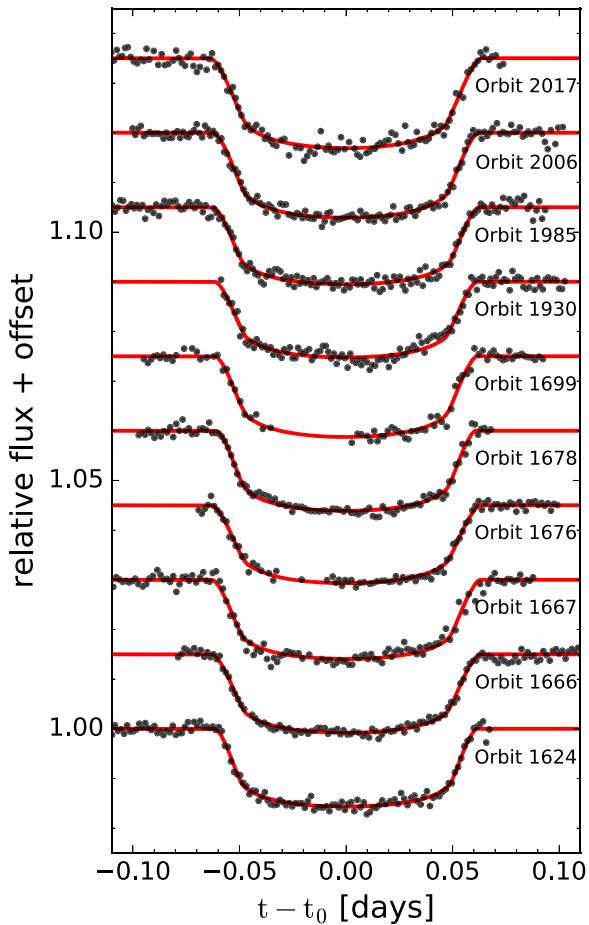


Figure 1. Transit light curves of WASP-12b, based on r' -band observations with the FLWO 1.2 m telescope. The red curves are based on the best-fitting model. The number on the right side of each light curve is the orbit number relative to a fixed reference orbit.

technique of Deming et al. (2015). We selected a grid of pixels surrounding the stellar image and divided each pixel value by the total flux in that exposure. The intention of this normalization procedure is to eliminate the information from the astrophysical signal (which affects all the pixels), leaving behind only the changes due to pointing fluctuations and differences in pixel sensitivity. Following Equation (4) of Deming et al. (2015), we modeled the light curve as a linear combination of the normalized pixel values $\hat{P}_i(t)$, a time-dependent trend $ft + gt^2$ that accounts for any phase curve variation or long-term instrumental artifacts, a constant offset h , and a geometric eclipse model $E(t)$ with depth D :

$$F_{\text{calc}}(t) = \sum_{i=1}^N c_i \hat{P}_i(t) + ft + gt^2 + h + DE(t). \quad (1)$$

This model could be extended to include cross-terms between the \hat{P}_i terms and the eclipse model, or higher-order terms in the pixel fluxes (Luger et al. 2016), but we chose not to do so, given the small values of $\sum c_i \hat{P}_i$ (< 0.01) and the eclipse depth (~ 0.005). For a given set of eclipse parameters, we used the *batman* code (Kreidberg 2015) to calculate $E(t)$. We used linear regression to solve Equation (1) for the coefficients c_i , f , g , and D that provide the best fit to the data $F_{\text{obs}}(t)$.

To speed up computations, it is helpful to reduce the data volume by binning the data in time. Deming et al. (2015) found that the optimized values of the coefficients c_i sometimes depend on the size of the time bins, which they attributed to time-correlated noise. They recommended choosing a bin size that minimizes the amplitude of correlated noise on the timescale of the eclipse. We determined this optimal bin size as follows. We obtained an initial estimate for the occultation time by fitting the unbinned data with a model in which all of the eclipse parameters (apart from the occultation time) were fixed to the values found by Collins et al. (2017). Then, using a fixed eclipse model with this occultation time, we determined the coefficients c_i , f , g , h , D for time-binned light curves, with bin sizes ranging from 2 to 60 exposures (4–120 s). In each case, we examined the residuals by binning them and computing the standard deviation. For uncorrelated noise, the residuals should scale approximately as $N^{-1/2}$ where N is the number of exposures per bin. We identified the optimal case as the one for which the residuals best match this expectation. As a further degree of optimization, we repeated this procedure for each choice of aperture radius, and selected the radius that led to the smallest standard deviation of the residuals. Table 2 gives the optimal set of photometric parameters for each observation, while the light curves are provided in Table 1.

After adopting the optimal aperture and bin size for each of the four observations, we jointly fitted all of the *Spitzer* data using a single eclipse model. This time, all of the eclipse parameters were allowed to vary, subject to prior constraints. We placed Gaussian priors on the orbital inclination I , planet-to-star radius ratio R_p/R_* , and orbit-to-star radius ratio a/R_* , based on the best-fit values and uncertainties reported by Collins et al. (2017), shown in Table 3. These parameters are sufficient to describe the loss of light as a function of the planet’s position on the stellar disk. To specify the loss of light as a function of time for each event, the timescale R_*P/a must also be specified (see Equation (19) of Winn 2010). We did so by holding P fixed at the value 1.09142 days, but importantly, we did not require the interval between occultations to be equal to 1.09142 days. We allowed the occultation midpoints and depths to be freely varying parameters.

Table 2 gives the final fit eclipse times and depths, while Table 3 gives the remaining fit results. The timing precision ranged from 1.0 to 1.3 minutes, which is similar to the results that were achieved by Deming et al. (2015) and Patra et al. (2017) for the same star. Figure 2 shows all four detrended *Spitzer* light curves, along with the best-fitting eclipse model curves.

3.2. WIRC Observations

An occultation of WASP-12b was also observed with the Wide-Field Infrared Camera (WIRC, Wilson et al. 2003) on the Hale 200 inch telescope at Palomar Observatory on 2017 March 18. This observation was made in the K_s band using a new Hawaii-II detector installed on WIRC in 2017 January (Tinyanont et al. 2019) and a near-infrared Engineered Diffuser (Stefansson et al. 2017). We obtained 1828 images with an exposure time of 2 s, spanning 5 hr.

Each image was corrected for dark current, flat field, and bad pixels with the WIRC Data Reduction Pipeline (Tinyanont et al. 2019). We performed circular-aperture photometry of WASP-12 and five comparison stars following the procedure

Table 2
New Occultation Midpoints and Depths

Source	<i>Spitzer</i>				WIRC	H19 ^a	V19 ^b
	2019 Jan 16	2019 Jan 20	2019 Jan 24	2019 Feb 2			
UT Date	2019 Jan 16	2019 Jan 20	2019 Jan 24	2019 Feb 2	2017 Mar 18	2017 Jan 16	2019 Jan 2
Orbit Number	2010	2014	2018	2026	1397	1341	1997
Midpoint ^c	58499.75572	58504.11988	58508.48459	58517.21641	57830.7139	57769.5957	58485.5642
Timing Uncertainty	0.00077	0.00087	0.00091	0.00074	0.0011	0.0014	0.0014
Eclipse Depth (ppm)	4720 ⁺²⁸⁹ ₋₂₇₉	4243 ⁺²⁷⁰ ₋₂₆₅	3601 ⁺²⁶¹ ₋₂₆₂	4632 ⁺²⁶⁶ ₋₂₅₈	3232 ⁺¹¹⁰ ₋₁₁₂	1089 ⁺⁷² ₋₇₁	1095 ⁺¹⁷⁵ ₋₁₇₆
Photometric band	Spitzer 4.5 μ m				K_s	i'	V
Aperture radius (pixels)	2.3	2.4	2.1	2.0
Bin size (exposures)	22	22	14	14

Notes.

^a Eclipse observed by Hooton et al. (2019).

^b Eclipse observed by von Essen et al. (2019).

^c Times given in BJD_{TDB}-2,400,000.

^d Aperture radius and bin sizes reported in this table only for the *Spitzer* observations.

Table 3
WASP-12 System Parameters based on *Spitzer* Occultations

Parameter	Prior ^a	Best-fit
Period (days)	1.09142	fixed
R_p/R_*	$\mathcal{G}(0.11785, 0.00054)$	0.11786 ± 0.00027
a/R_*	$\mathcal{G}(3.039, 0.034)$	3.036 ± 0.014
I (deg)	$\mathcal{G}(83.37, 0.7)$	83.38 ± 0.3
e	0.0	fixed
ω (deg)	0.0	fixed

Note.

^a Based on values from Collins et al. (2017). We used Gaussian priors denoted by $\mathcal{G}(\mu, \sigma)$.

described by Vissapragada et al. (2019). A global background was subtracted from each image using iterative 3σ clipping of the flux values, while a local background was determined for each star using annuli with inner and outer radii of 20 and 50 pixels. Optimizing the pipeline over various aperture sizes found a best circular-aperture radius of 9 pixels. The resulting light curve is provided in Table 1. We modeled the flux time series for WASP-12 as the product of an eclipse model $E(t)$ and a model of systematic effects, consisting of a linear function of time and a linear combination of the fluxes from the five comparison stars:

$$M(t) = \left(ft + \sum_{i=1}^5 c_i S_i(t) \right) \times E(t). \quad (2)$$

We used linear regression to solve for the coefficients in the systematics model, given a choice of parameters for the eclipse model (Vissapragada et al. 2019).

Figure 3 shows the resulting light curve after removing the best-fitting model for the systematic effects. The latter part of the observation was affected by intermittent cirrus clouds, causing sudden and large-amplitude fluctuations in the measured fluxes and leading to larger scatter in the detrended light curve. For this reason, we chose not to fit the data that were obtained during that time period (the gray region in Figure 3). This meant that the egress time and the total transit duration could not be determined from the WIRC data alone. Instead, we held fixed the geometric eclipse parameters at the

values taken from the best-fitting model of the *Spitzer* data (Table 3). We allowed the eclipse depth and midpoint to vary freely. The results of this fit are given in Table 2, and plotted as a red curve in Figure 3. When the entire light curve is fitted, instead of masking out the latter part of the transit, the derived mideclipse time shifts by 0.5σ and has a formal uncertainty that is a factor of 2 smaller.

3.3. Reanalysis of Previous Data

Two other groups have recently reported on observations of occultations of WASP-12b. Hooton et al. (2019) detected the occultation at the 7σ level using the Isaac Newton Telescope on La Palma, in 2017 January. Separately, von Essen et al. (2019) observed three occultations of WASP-12b in 2019 January with the 2.5 m Nordic Optical Telescope (NOT). While neither of these authors published the mideclipse times of their observations, they kindly provided us the light curves. For the observations by von Essen et al. (2019), only the first occultation was securely detected. We only reanalyzed the data from this event. We followed the same detrending procedures that are described in their papers to refit the light curves, holding the eclipse parameters fixed at the values from the best-fitting model to the *Spitzer* data (apart from the eclipse depth and midpoint). We were able to reproduce their results for the eclipse depths. Table 2 gives the corresponding mideclipse times.

4. Radial-velocity Observations

Knutson et al. (2014) presented radial-velocity measurements of WASP-12 spanning about 6 yr, using the High Resolution Echelle Spectrometer (HIRES; Vogt et al. 1994) on the Keck I telescope. As part of this long-term program, we have obtained three new observations of WASP-12 extending the time baseline by 5 yr. These new observations were reduced with the standard pipeline of the California Planet Search (CPS; Howard et al. 2010). Table 4 gives the complete set of radial-velocity data. The longer baseline is important for detecting any acceleration of the WASP-12 system along the line of sight, which would lead to apparent changes in orbital period due to the Rømer effect.

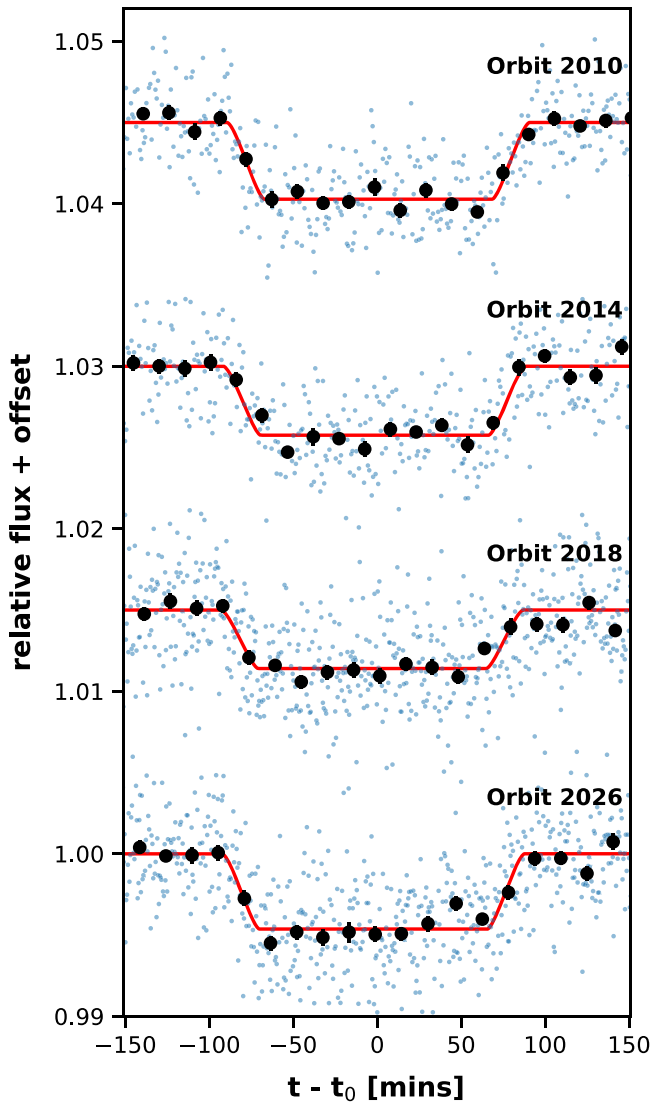


Figure 2. Occultations of WASP-12b, based on $4.5 \mu\text{m}$ observations with the *Spitzer Space Telescope*. The data were obtained and analyzed with a time sampling of 2 s, but for display purposes are shown here after averaging in time. For the top two light curves, the small blue points represent bins of 10 exposures (20 s). For the bottom two light curves, the small blue points represent bins of 14 exposures (28 s). In all cases, the large black points represent bins of 400 exposures (800 s). The red curves are based on the best-fitting model. As in Figure 1, each light curve is labeled with an orbit number relative to a fixed reference orbit.

5. Analysis

We compiled all of the available transit and occultation times, including the new data presented in Sections 2 and 3 as well as from the literature. We decided to include only those times that were based on fitting the data from a single event (as opposed to fitting multiple events and requiring periodicity), for which the midpoint was allowed to be a free parameter, and for which the time system of the measurement was clearly documented. Most of these times had already been compiled by Patra et al. (2017); we added 38 new transit times and 7 new occultation times. Table 5 gives all of the timing data. We emphasize that the times in Table 5 are all in the BJD_{TDB} system, and that no adjustment was made to the observed occultation times to account for the light-travel time across the diameter of the WASP-12 orbit. When analyzing the data, as

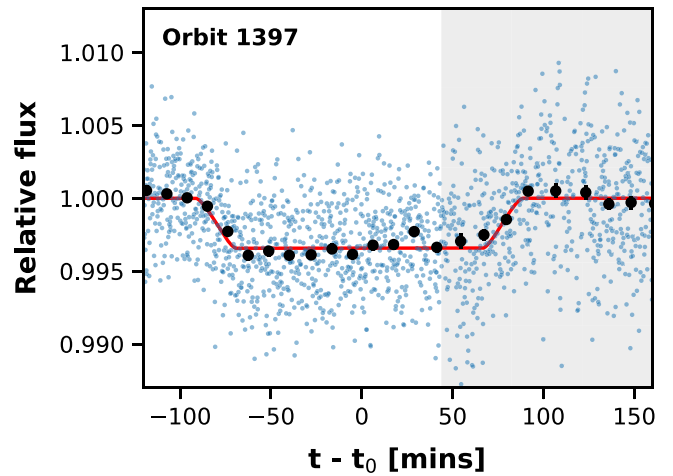


Figure 3. Occultation light curve observed by WIRC (blue points). Detrending was performed with the entire light curve, but the second half of the light curve (shaded gray) was excluded when we performed the final fit to the eclipse model. The best-fitting eclipse model to the truncated light curve is shown in red. Black points show the light curve binned to 70 exposures for clarity. Error bars are not shown for the unbinned data.

Table 4
HIRES Radial Velocity Measurements

Time BJD_{TDB}	RV (m s^{-1})	$\sigma(\text{RV})$ (m s^{-1})
2455521.959432	-136.635	2.534
2455543.089922	5.728	2.919
2455545.983884	-162.390	2.822
2455559.906718	141.616	2.345
2455559.917563	115.818	2.727
2455559.927852	111.001	3.186
2455636.843302	-143.932	2.627
2455671.769904	-107.997	2.446

(This table is available in its entirety in machine-readable form.)

described below, we did account for the light-travel time by subtracting $2a/c = 22.9 \text{ s}$ from the observed occultation times.⁹

5.1. Timing Analysis

Following Patra et al. (2017), we fitted three models to the timing data. The first model assumes the orbital period to be constant:

$$\begin{aligned}
 t_{\text{tra}}(N) &= t_0 + NP \\
 t_{\text{occ}}(N) &= t_0 + \frac{P}{2} + NP,
 \end{aligned} \tag{3}$$

where N is the number of orbits from a fixed reference orbit,¹⁰ while t_0 is the midtransit time of this reference orbit.

⁹ In the process of compiling the data, we found that Table 1 of Patra et al. (2017) has an error: except for the *Spitzer* data they presented for the first time, all of the reported occultation times are wrong by an offset of 50.976 s, due to a software bug that arose from confusion over whether the light-time correction had already been applied. This error only affected the values printed in the table, and not the timing analysis or any of the results reported by Patra et al. (2017).

¹⁰ We chose the reference orbit as the one with midtransit time close to $\text{BJD}_{\text{TDB}} \approx 2456305.45$, consistent with the choice made in Patra et al. (2017).

Table 5
WASP-12b Transit and Occultation Times

Event	Midtime BJD _{TDB}	Error days	Orbit No.	Source
tra	2454515.52496	0.00043	−1640	H09 ^a
occ	2454769.28190	0.00080	−1408	Ca11
occ	2454773.64810	0.00060	−1404	Ca11
tra	2454836.40340	0.00028	−1346	C13
tra	2454840.76893	0.00062	−1342	Ch11
tra	2455140.90981	0.00042	−1067	C17
tra	2455147.45861	0.00043	−1061	M13
tra	2455163.83061	0.00032	−1046	C17

Notes.^a The transit of orbit −1640 observed by H09 was reanalyzed by M13.^b The occultation of orbit −722 observed by D15 was reanalyzed by P17.

References. H09—Hebb et al. (2009), C13—Copperwheat et al. (2013), C15—Croll et al. (2015), C17—Collins et al. (2017), Ca11—Campo et al. (2011), Ch11—Chan et al. (2011), Co12—Cowan et al. (2012), Cr12—Crossfield et al. (2012), D15—Deming et al. (2015), F13—Föhning et al. (2013), H19—Hooton et al. (2019), K15—Kreidberg et al. (2015), M13—Maciejewski et al. (2013), M16—Maciejewski et al. (2016), M18—Maciejewski et al. (2018), O19—Öztürk & Erdem (2019), P17—Patra et al. (2017), P19—Patra et al. (2019), S12—Sada et al. (2012), S14—Stevenson et al. (2014), V19—von Essen et al. (2019).

(This table is available in its entirety in machine-readable form.)

The second model assumes the orbital period to be changing uniformly with time:

$$\begin{aligned}
 t_{\text{tra}}(N) &= t_0 + NP + \frac{1}{2} \frac{dP}{dN} N^2 \\
 t_{\text{occ}}(N) &= t_0 + \frac{P}{2} + NP + \frac{1}{2} \frac{dP}{dN} N^2.
 \end{aligned} \quad (4)$$

The third model assumes the planet has a nonzero eccentricity e and its argument of pericenter ω is precessing uniformly: (Giménez & Bastero 1995):

$$\begin{aligned}
 t_{\text{tra}}(N) &= t_0 + NP_s - \frac{eP_a}{\pi} \cos \omega(N) \\
 t_{\text{occ}}(N) &= t_0 + \frac{P_a}{2} + NP_s + \frac{eP_a}{\pi} \cos \omega(N) \\
 \omega(N) &= \omega_0 + \frac{d\omega}{dN} N \\
 P_s &= P_a \left(1 - \frac{1}{2\pi} \frac{d\omega}{dN} \right),
 \end{aligned} \quad (5)$$

where P_s is the sidereal period and P_a is the anomalistic period.

In all three cases, we found the best-fitting model parameters by minimizing χ^2 . We again used the `emcee` code to perform an MCMC sampling of the posterior distribution in parameter space, given broad uniform priors on all the parameters. We ran the MCMC with 100 walkers, discarding the first 40% of the steps as burn-in and running the code for >10 autocorrelation times. We also double-checked convergence by inspecting the posteriors and computing the Geweke scores for each chain (Geweke 1992). Table 6 gives the fit results.

As was already shown by Maciejewski et al. (2016) and Patra et al. (2017), the constant period model does not fit the data. The minimum value of χ^2 is 380.7 with 156 degrees of

Table 6
Timing Model Fit Parameters

Parameter	Value (Uncertainty)
Constant Period Model	
Period, P (days)	1.091419649(25)
Midtransit Time of Reference Orbit, t_0	2456305.455521(26)
N_{dof}	156
χ^2_{min}	380.745
BIC	390.871
Orbital Decay Model	
Period, P (days)	1.091420107(42)
Midtransit Time of Reference Orbit, t_0	2456305.455809(32)
Decay Rate, dP/dN (days/orbit)	$-10:04(69) \times 10^{-10}$
N_{dof}	155
χ^2_{min}	167.566
BIC	182.754
Apsidal Precession Model	
Sidereal Period, P_s (days)	1.091419633(81)
Midtransit Time of Reference Orbit, t_0	2456305.45488(12)
Eccentricity, e	0.00310(35)
Argument of Periastron, ω_0 (rad)	2.62(10)
Precession Rate, $d\omega/dN$ (rad/orbit)	0.000984(+70, −61)
N_{dof}	153
χ^2_{min}	179.700
BIC	205.013

Note. Uncertainties in parentheses are the 1σ confidence intervals in the last two digits.

freedom. Figure 4 shows the residuals. Also plotted are the best-fitting model curves for the orbital decay and apsidal precession models. The best-fitting orbital decay model has $\chi^2_{\text{min}} = 167.6$, while the best-fitting apsidal precession model has $\chi^2_{\text{min}} = 179.7$. Thus, while both models fit the data much better than the constant-period model, the orbital decay model is preferred. The difference in χ^2 is 12.1. Patra et al. (2017) also found a preference for orbital decay, but with a weaker statistical significance ($\Delta\chi^2 = 5.5$). Most of the increase in $\Delta\chi^2$ is from the newest *Spitzer* observations of occultations, for which the midpoints are consistent with the predictions of the orbital decay model, but occurred earlier than would be expected based on the apsidal precession model.

Our confidence that orbital decay is a better description of the data is enhanced by the fact that the orbital decay model has only three free parameters while the apsidal precession model has five free parameters. A commonly used way to reward a model for fitting the data with fewer free parameters is to compare models with the Bayesian Information Criterion (BIC; Schwarz 1978):

$$\text{BIC} = \chi^2 + k \log n, \quad (6)$$

where k is the number of free parameters, and n is the number of data points. In this case, the BIC favors the orbital decay model by $\Delta(\text{BIC}) = 22.3$. The interpretation of this number is not completely straightforward, but if we assume the posterior distribution of all the parameters to be a multivariate Gaussian function, then there is a simple relation between ΔBIC and the

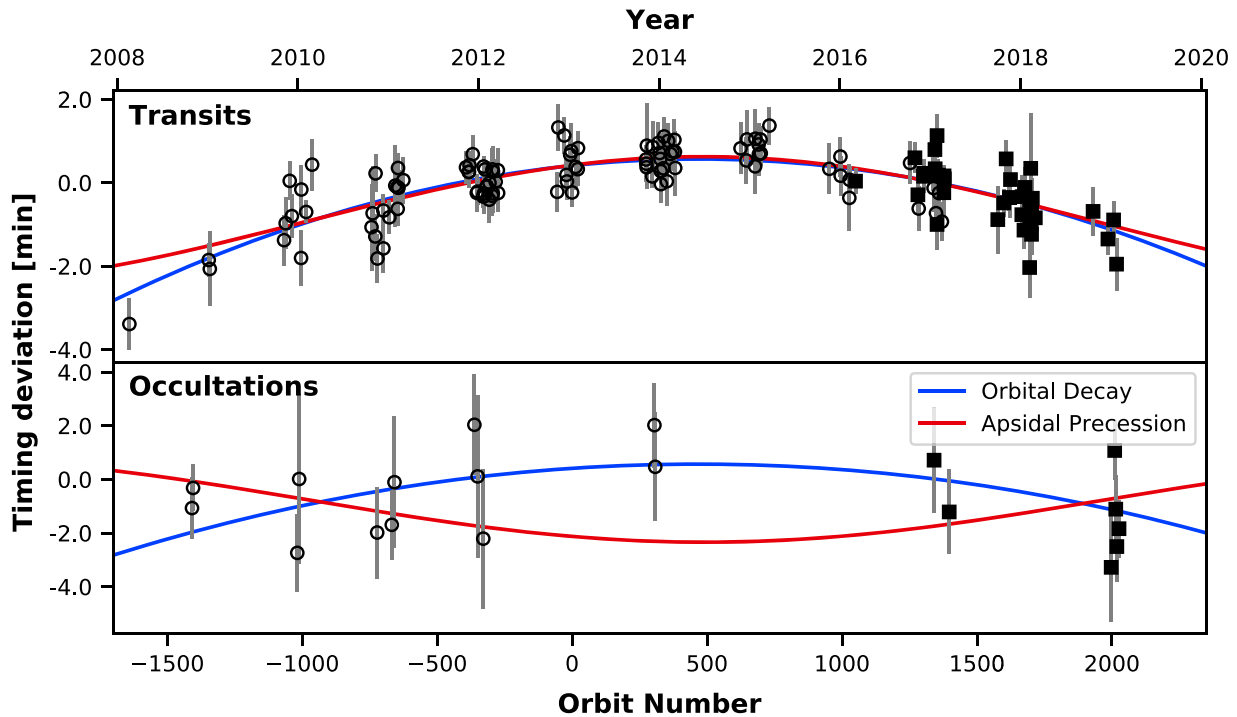


Figure 4. Transit and occultation timing residuals, after subtracting the best-fitting constant-period model. Open circles denote those points previously compiled in Patra et al. (2017); solid squares are the new transit and occultation times compiled in this work. The blue line shows the expected residuals for the best-fitting orbital decay model, while the red line shows the best-fitting apsidal precession model.

Bayes factor B :

$$B = \exp[-\Delta(\text{BIC})/2] = 70,000, \quad (7)$$

representing an overwhelming preference for the orbital decay model.

5.2. Radial Velocity Analysis

5.2.1. Rømer Effect

If the center of mass of the star–planet system is accelerating along the line of sight with a magnitude \dot{v}_r , then the apparent period of the hot Jupiter would be observed to change due to the Rømer effect:

$$\frac{\dot{P}}{P} = \frac{\dot{v}_r}{c}.$$

If we insert the measured values of P and \dot{P} for WASP-12 into this equation, the implied acceleration is $\dot{v}_r = 0.25 \text{ m s}^{-1} \text{ day}^{-1}$. This is more than an order of magnitude larger than the 2σ upper limit of $0.019 \text{ m s}^{-1} \text{ day}^{-1}$ that Patra et al. (2017) obtained by fitting the previously available radial-velocity data. Here, we use the newly obtained radial-velocity data to place an even more stringent upper limit.

In addition to the HIRES radial velocities from Knutson et al. (2014) and described in Section 4, we analyzed the data obtained with the SOPHIE spectrography by Hebb et al. (2009) and Husnoo et al. (2011), as well as data obtained with the HARPS-N spectrograph by Bonomo et al. (2017). We allowed for a constant velocity offset and a “jitter” value specific to each spectrograph. We also excluded the data points obtained during transits, to avoid having to model the Rossiter–McLaughlin effect. We used the `radvel` code (Fulton et al. 2018) to fit a model consisting of the sum of a sinusoidal

function (representing the circular orbit of the planet) and a linear function of time (representing a constant radial acceleration). We fixed the period and time of conjunction to the values from the best-fitting constant period timing model (Table 6).

Figure 5 shows the residuals, after subtracting the best-fitting model. Any line-of-sight acceleration must have an amplitude $|\dot{v}_r| < 0.005 \text{ m s}^{-1} \text{ day}^{-1}$, at the 2σ level. This is a factor of four improvement over the constraints reported by Patra et al. (2017), and two orders of magnitude smaller than the value that would be observed if the observed period derivative were entirely due to the Rømer effect. Thus, we can dismiss the Rømer effects as a significant contributor to the observed period change.¹¹

5.2.2. Orbital Eccentricity

The apsidal precession hypothesis requires that the orbit is slightly eccentric. In the best-fitting timing model, the eccentricity is about 0.003. This raises a theoretical problem, because the expected timescale for tidal circularization is about 0.5 Myr (Patra et al. 2017). Thus, if apsidal precession were taking place, there needs to be some mechanism for maintaining the eccentricity at the level of 10^{-3} despite the expectation of rapid tidal circularization.

For WASP-12b, the radial-velocity data are compatible with a circular orbit, but they are not precise enough to rule out an orbital eccentricity at the level of 10^{-3} . Indeed, when we refitted the radial-velocity data allowing the orbit to be eccentric, we found that the best-fitting model implies a larger eccentricity:

¹¹ Based on a reanalysis of the SOPHIE and HARPS spectra, Baluev et al. (2019) reported a radial-velocity trend of $-7.5 \pm 2.2 \text{ m s}^{-1} \text{ yr}^{-1}$ or $-0.021 \pm 0.006 \text{ m s}^{-1} \text{ day}^{-1}$. This is four times larger than our upper limit, and is therefore ruled out. The most recent Keck/HIRES data were helpful in this regard.

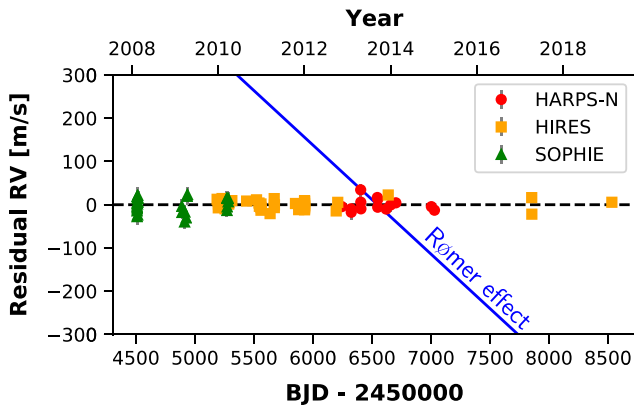


Figure 5. Radial velocity residuals after subtracting the best-fitting sinusoidal model. No significant trends are seen in the residuals. The blue line has the slope that would have been observed, if the Rømer effect were solely responsible for the observed period derivative.

$\sqrt{e} \cos \omega_* = -0.0004 \pm 0.029$, $\sqrt{e} \sin \omega_* = -0.175^{+0.028}_{-0.024}$, and $e = 0.0317 \pm 0.0087$. This is consistent with the previous reports of a nonzero eccentricity by Knutson et al. (2014) and Husnoo et al. (2011).

However, we think that this is a spurious result. The clue is that the best-fitting argument of pericenter is aligned nearly exactly with the line of sight: $\omega = -89.9^{+9.7}_{-9.2}$ deg. Most likely, the orbit is circular, and the apparently nonzero eccentricity is due to an unmodeled systematic effect. A good candidate for this effect is the tidal distortion of the host star. As pointed out by Arras et al. (2012), the tidal bulge raised by a hot Jupiter can cause an apparent radial-velocity signal with a period equal to half of the orbital period. This would lead to a second harmonic in the radial-velocity data that can be mistaken for the signal of an eccentric orbit. In particular, Arras et al. (2012) showed that a planet on a circular orbit would appear to have a nonzero orbital eccentricity and an argument of pericenter $\omega = -90$ deg. Furthermore, Arras et al. (2012) predicted that for the specific case of WASP-12, the fictitious eccentricity would have an amplitude on the order of 0.02. Both of these predictions are consistent with what has been observed.¹²

5.2.3. Joint RV-timing Fit

In principle, the radial-velocity signal should also be affected by either orbital decay or apsidal precession. A change in the orbital period would affect the RV signal via the true anomaly ν . We computed the radial-velocity signal of a planet with a constant and decaying period using the parameters in Table 6. Over the 9 yr timespan of the HIRES radial-velocity observations, we found that the maximum deviation between the two models is ~ 10 m s⁻¹.

As for apsidal precession, Csizmadia et al. (2019) presented a formula for the associated RV signal:

$$\text{RV} = K \left[e \cos \omega(t) + \cos(\nu + \omega(t)) + \frac{\dot{\omega} (1 - e^2)^{3/2} \cos(\nu + \omega(t))}{n (1 + e \cos \nu)} \right]$$

$$\omega(t) = \omega_0 + \dot{\omega}(t - t_0), \quad (8)$$

¹² At the Extreme Solar Systems IV conference, in Reykjavik, Iceland (2019 August 19–23), G. Maciejewski presented further evidence for the effect of the tidal bulge in the radial-velocity data for WASP-12.

where $n \equiv 2\pi/P$ is the mean motion. Based on this equation, along with the precession period from the best-fitting apsidal precession model, we found that the maximum deviation between the RV signal of a precessing orbit with parameters in Table 6 and a circular model would be ~ 6 m s⁻¹ over a decade. We note that Csizmadia et al. (2019) claimed that apsidal precession would result in residuals on the order of K_{orb} ; however, that only holds if the anomalistic period could be determined independently. In reality, the anomalistic period would need to be determined using the same data, and the residuals would be on the order of $e K_{\text{orb}}$.

In both cases, there should be small but potentially measurable effects on the RV data. We tried fitting the timing and RV data sets jointly, but the results were essentially unchanged. In particular, the RV data did not alter the ΔBIC between the orbital decay and apsidal precession models. This is likely because the RV observations at later times are sparsely sampled, preventing these small deviations from being measured effectively. Furthermore, the RV jitter of WASP-12 in the HIRES observations is $\sigma_{\text{jit}} \sim 10$ m s⁻¹, a similar magnitude to the decay or precession RV signal. Future RV measurements could be helpful, but only if the RV systematic effects are better understood, including the tidal effect described in Section 5.2.2.

6. Discussion

Since the work of Patra et al. (2017), evidence has continued to mount that the orbit of WASP-12b is decaying, as opposed to apsidally precessing. The difference in χ^2 between the orbital decay and apsidal precession models has grown from 5.5 to 12.1, and the difference in the BIC has widened from 14.9 to 22.3. Also noteworthy is that as new data have become available, the best-fitting orbital decay parameters have remained the same, while the best-fitting apsidal precession parameters have changed significantly. Our measurement of $dP/dN = -10.0^{+0.68}_{-0.69} \times 10^{-10}$ days/epoch is consistent with the rate of $(-10.2 \pm 1.1) \times 10^{-10}$ days/orbit reported by Patra et al. (2017), and with the rate of $dP/dN = (-9.67 \pm 0.73) \times 10^{-10}$ days/orbit reported by Maciejewski et al. (2018). In contrast, between 2017 and our study, the best-fitting orbital eccentricity in the precession model has increased by a factor of 1.5 ± 0.4 and the best-fitting precession period has increased by a factor of 1.4 ± 0.2 .

We are now ready to conclude that WASP-12b is the first planet known to be undergoing orbital decay. The timescale over which the orbit is shrinking is

$$\tau = \frac{P}{|\dot{P}|} = 3.25^{+0.24}_{-0.21} \text{ Myr.}$$

Given that the host star appears to be at least 1 Gyr old, it may seem remarkable that we are observing the planet so close to the time of its destruction. If we were observing a single planet at a random moment within its 1 Gyr lifetime, the chance of catching it within the last 3 Myr would be only 0.3%. However, ground- and space-based surveys have searched hundreds of thousands of stars for hot Jupiters. Given that hot Jupiters occur around $\sim 1\%$ of stars and have a transit probability of $\sim 10\%$, we might expect to find $500,000 \times 1\% \times 10\% \times 0.3\% \sim 2$ planets as close to the end of their lives as is implied by the decay rate of WASP-12b.

The orbital energy and angular momentum are both decreasing, at rates of

$$\frac{dE}{dt} = \frac{(2\pi)^{2/3} M_p \left(\frac{GM_*}{P} \right)^{2/3}}{3} \frac{1}{P} \frac{dP}{dt} = -5 \times 10^{23} \text{ Watts}, \quad (9)$$

$$\frac{dL}{dt} = \frac{M_p}{3(2\pi)^{1/3}} \left(\frac{GM_*}{P} \right)^{2/3} \frac{dP}{dt} = -7 \times 10^{27} \text{ kg m}^2 \text{ s}^{-2}, \quad (10)$$

where we have used the stellar and planetary masses $M_* = 1.4 \pm 0.1 M_\odot$, $M_p = 1.47 \pm 0.07 M_J$, from Collins et al. (2017). While it would still be useful to reduce the uncertainties in the timing model by observing more transits and occultations, there are more interesting questions regarding the mechanism by which the orbit is losing energy and angular momentum, and what sets WASP-12b apart from the other hot Jupiters for which orbital decay has not been detected.

6.1. Tidal Orbital Decay

The possibility discussed in the Introduction is that the angular momentum is being transferred directly to the star through the gravitational torque on the star’s tidal bulge, and the energy is being dissipated inside the star as the tidal oscillations are converted into heat. In the “constant phase lag” model of Goldreich & Soter (1966), assuming that the planet’s mass stays constant, the decay rate is

$$\dot{P} = -\frac{27\pi}{2Q_*} \left(\frac{M_p}{M_*} \right) \left(\frac{R_*}{a} \right)^5,$$

where Q'_* is the star’s “modified tidal quality factor,” defined as the quality factor Q_* divided by $2/3$ of the Love number k_2 . Inserting the measured decay rate, we obtain for WASP-12 a tidal quality factor of

$$Q'_* = 1.75^{+0.13}_{-0.11} \times 10^5.$$

This result for Q'_* is lower than most of the estimates in the literature, which are based on less direct observations. By analyzing the eccentricity distribution of stellar binaries, Meibom & Mathieu (2005) found Q'_* to be in the range from 10^5 to 10^7 , while similar studies applied to hot Jupiter systems by Jackson et al. (2008) and Husnoo et al. (2012) found $Q'_* = 10^{5.5} - 10^{6.5}$. Hamer & Schlaufman (2019) found that hot Jupiter host stars are kinematically younger than similar stars without hot Jupiters, and interpreted the result as evidence for the tidal destruction of hot Jupiters, finding $Q'_* = 10^6 - 10^{6.5}$. Collier Cameron & Jardine (2018) modeled the orbital period distribution of the hot Jupiter population and found $Q'_* = 10^7 - 10^8$. Penev et al. (2012) modeled the star/planet tidal interactions in selected systems and also found $Q'_* > 10^7$. However, these studies assumed Q s to be a universal constant, even though one would expect it to depend on forcing frequency and perhaps many other parameters. Penev et al. (2018) updated and expanded the approach of system-by-system modeling to allow for frequency dependence, finding that Q'_* ranges from 10^5 to 10^7 for orbital periods of 0.5–2 days (Penev et al. 2018).

If tidal dissipation is responsible for the orbital decay of WASP-12, then the dissipation rate is higher than would have been expected according to these earlier studies. The physical mechanism for such rapid dissipation is unclear. Attempts to

compute the tidal quality factor from physical principles for either the equilibrium or dynamical tide generally find larger values of Q'_* , from 10^7 to 10^{10} (as reviewed by Ogilvie 2014). Weinberg et al. (2017) argued that WASP-12 could be a subgiant star, in which case nonlinear wave-breaking of the dynamical tide near the stellar core would lead to efficient dissipation and $Q'_* \sim 2 \times 10^5$. However, Bailey & Goodman (2019) examined this possibility and found that the observed properties of WASP-12 are more compatible with the expected properties of a main-sequence star rather than a subgiant.

Millholland & Laughlin (2018) proposed an alternate hypothesis, in which WASP-12b is in a spin-orbit resonance with an external perturber, allowing it to maintain a large obliquity and giving rise to obliquity tides. The ongoing dissipation of obliquity tides might be strong enough to explain the observed decay rate. While such a hypothetical perturber cannot yet be ruled out, this scenario calls for a specific system architecture with a misaligned perturber just below the limits of detection.

6.2. Roche Lobe Overflow

The Roche limit for a close-orbiting planet can be expressed as a minimum orbital period depending on the density distribution of the planet (Rappaport et al. 2013). For WASP-12b, with a mean density of 0.46 g cm^{-3} , the Roche-limiting orbital period is 14.2 hr assuming the mass of the planet to be concentrated near the center, and 18.6 hr in the opposite limit of a spherical and incompressible planet. The true orbital period of 26 hr is longer than either of these limits, implying that the planet is not filling its Roche lobe. This simple comparison does not take into account the planet’s tidal distortion, which would lead to a longer period for the Roche limit, but probably not as long as 26 hr.

Nevertheless, there may exist an optically thin exosphere or wind that does fill the Roche lobe. Ultraviolet observations of the WASP-12 system indicate that the planet is surrounded by a cloud of absorbing material that is larger than the Roche lobe (Fossati et al. 2010; Haswell et al. 2012; Nichols et al. 2015). Recent infrared phase curve observations of the WASP-12 system also corroborate the idea that gas is being stripped from the planet (Bell et al. 2019). The mass-loss rate is not measured directly (Haswell 2018), but models of this process suggest it could be as high as $\sim 3 \times 10^{14} \text{ g s}^{-1}$, corresponding to $M_p/\dot{M} \approx 300 \text{ Myr}$ (Lai et al. 2010; Jackson et al. 2017). This mass-loss timescale, while longer than the tidal decay timescale, is still short relative to the age of the star. Putting this evidence together with the observed changes in orbital period, it seems that tidal orbital decay has brought the planet close enough to initiate Roche lobe overflow of the planet’s tenuous outer atmosphere.

The escaping mass bears energy and angular momentum, which can lead to changes in the orbital period separate from the effects of the tidal bulge of the star. To assess whether or not the escaping mass bears enough angular momentum to be relevant for period changes, we need to know more about the flow of mass away from the planet. We would expect the gas to flow out from the inner Lagrange point, with lower specific angular momentum than the rest of the planet. As a result, the planet’s specific angular momentum would rise, causing its orbit to widen. In this scenario, the rate of period decrease that we have measured would be the result of a competition between tidally driven decay and mass-loss-driven growth.

Jia & Spruit (2017) presented an expression relating the change in semimajor axis to the mass-loss rate:

$$\frac{\dot{a}}{a} = \frac{2}{1+q} \frac{\dot{M}_p}{M_p} \left[\frac{x_{L1}^2}{x_p^2} (1 - \epsilon) + q^2 - 1 \right] > 0, \quad (11)$$

where q is the planet–star mass ratio, x_{L1} , x_p are the distances from the L1 point and planet to the system center of mass, and ϵ parameterizes the fraction of angular momentum that is transferred back to the planet from the outflowing gas. Using the mass-loss rate estimated by Lai et al. (2010) and Jackson et al. (2017), and assuming no angular momentum transfer back to the planet ($\epsilon = 0$), this yields

$$\frac{\dot{P}}{P} \approx 3 \frac{\dot{M}_p}{M_p} \quad (12)$$

$$\dot{P} \approx 1 \text{ ms yr}^{-1}. \quad (13)$$

Under these assumptions, the mass loss from the planet causes a period increase about 30 times smaller than the observed period change for WASP-12b, and is unlikely to be slowing down the planet’s orbital decay.

On the other hand, if gas flows out of the L2 point, there could be a net loss in angular momentum from the planet, hastening any tidally driven decay of the orbit. Valsecchi et al. (2015) examined this process and found that the orbital period begins to shrink only in the final stages of mass loss, when the remaining mass of the planet is dominated by the dense core. This is not the current situation of WASP-12b, given its Jovian mass and low mean density. Furthermore, Jia & Spruit (2017) found that even in such a scenario, the mass loss from L1 continues to dominate over the outflow from L2, leading to continued expansion of the orbit. In either case, it seems unlikely that the mass loss from WASP-12b is contributing significantly to its orbital evolution.

7. Conclusion

We have presented new timing data for WASP-12b that have finally allowed us to determine that its orbit is decaying. We measured a shift in transit and occultation times of about 4 minutes over a 10 year period, corresponding to a period derivative of $\dot{P} = -29 \pm 2 \text{ ms yr}^{-1}$. This is the first time a hot Jupiter has been caught in the act of spiraling into its host star. It will likely be destroyed on a timescale of several million years.

The WASP-12 system will be observed by the *Transiting Exoplanet Survey Satellite* (*TESS*; Ricker et al. 2014) in Sector 20, from 2019 December to 2020 January. The new high-precision light curves from *TESS* will improve our measurement of Q'_* of WASP-12, as will any further transit or occultation observations in the future.

It will also be important to seek evidence for orbital decay in other systems. Already, it is clear that not all systems have the same effective value of Q'_* . For example, the hot Jupiter WASP-19b has an orbital period of 0.79 days, even shorter than that of WASP-12, and was predicted to be the most favorable system for measuring orbital decay (see, e.g., Valsecchi & Rasio 2014; Essick & Weinberg 2015). However, a recent analysis of transit times by Petrucci et al. (2019) shows that any period changes of WASP-19b are slower than 2.2 ms yr^{-1} , implying $Q'_* > 1.2 \times 10^6$, limits that are

incompatible with the observations of WASP-12. This may be because WASP-12 is a subgiant star, as advocated by Weinberg et al. (2017). The best way to understand if this is the case is to expand the collection of systems for which detections or period changes, or stringent upper limits, have been made. This will help to clarify the interpretation and check on the dependence of tidal dissipation rates on properties such as the planet mass and orbital period, and the stellar evolutionary state and rotation rate.

In the case of WASP-12b, it was only through more than a decade of combined photometric and spectroscopic observations that we were able to firmly distinguish the orbital decay scenario from other physical processes that can result in similar observational signatures. Similar monitoring of other hot Jupiters—and indeed, all types of planets—will be important in understanding these slow-acting but important physical processes that sculpt the architecture of exoplanetary systems.

We thank Jeremy Goodman and Luke Bouma for helpful discussions while preparing this manuscript. The authors gratefully acknowledge Leo Liu for helping obtain the WIRC observations. Work by S.W.Y and J.N.W was partly supported by the Heising-Simons Foundation. J.T.W. acknowledges support from NASA Origins of Solar Systems grant NNX14AD22G. The Center for Exoplanets and Habitable Worlds is supported by the Pennsylvania State University, the Eberly College of Science, and the Pennsylvania Space Grant Consortium. This research has made use of the VizieR catalog access tool, CDS, Strasbourg, France. The original description of the VizieR service was published in A&AS 143, 23. Some of the data presented herein were obtained at the W. M. Keck Observatory, which is operated as a scientific partnership among the California Institute of Technology, the University of California and the National Aeronautics and Space Administration. The Observatory was made possible by the generous financial support of the W. M. Keck Foundation. The authors wish to recognize and acknowledge the very significant cultural role and reverence that the summit of Maunakea has always had within the indigenous Hawaiian community. We are most fortunate to have the opportunity to conduct observations from this mountain.

Software: `astropy` (Astropy Collaboration et al. 2013, 2018); `emcee` (Foreman-Mackey et al. 2013; Goodman & Weare 2010); `radvel` (Fulton et al. 2018); `numpy` (Van Der Walt et al. 2011); `scipy` (Jones et al. 2001).

ORCID iDs

Samuel W. Yee  <https://orcid.org/0000-0001-7961-3907>
 Joshua N. Winn  <https://orcid.org/0000-0002-4265-047X>
 Heather A. Knutson  <https://orcid.org/0000-0002-0822-3095>
 Kishore C. Patra  <https://orcid.org/0000-0002-1092-6806>
 Shreyas Vissapragada  <https://orcid.org/0000-0003-2527-1475>
 Michael M. Zhang  <https://orcid.org/0000-0002-0659-1783>
 Matthew J. Holman  <https://orcid.org/0000-0002-1139-4880>
 Avi Shporer  <https://orcid.org/0000-0002-1836-3120>
 Jason T. Wright  <https://orcid.org/0000-0001-6160-5888>

References

- Astropy Collaboration, Price-Whelan, A. M., Sipőcz, B. M., et al. 2018, *AJ*, 156, 123
 Astropy Collaboration, Robitaille, T. P., Tollerud, E. J., et al. 2013, *A&A*, 558, A33

- Arras, P., Burkart, J., Quataert, E., & Weinberg, N. N. 2012, *MNRAS*, **422**, 1761
- Bailey, A., & Goodman, J. 2019, *MNRAS*, **482**, 1872
- Baluev, R. V., Sokov, E. N., Jones, H. R. A., et al. 2019, *MNRAS*, **490**, 1294
- Bell, T. J., Zhang, M., Cubillos, P. E., et al. 2019, *MNRAS*, **489**, 1995
- Bonomo, A. S., Desidera, S., Benatti, S., et al. 2017, *A&A*, **602**, A107
- Campo, C. J., Harrington, J., Hardy, R. A., et al. 2011, *ApJ*, **727**, 125
- Chan, T., Ingemyr, M., Winn, J. N., et al. 2011, *AJ*, **141**, 179
- Claret, A., & Bloemen, S. 2011, *A&A*, **529**, A75
- Collier Cameron, A., & Jardine, M. 2018, *MNRAS*, **476**, 2542
- Collins, K. A., Kielkopf, J. F., & Stassun, K. G. 2017, *AJ*, **153**, 78
- Copperwheat, C. M., Wheatley, P. J., Southworth, J., et al. 2013, *MNRAS*, **434**, 661
- Counselman, C. C. 1973, *ApJ*, **180**, 307
- Cowan, N. B., Machalek, P., Croll, B., et al. 2012, *ApJ*, **747**, 82
- Croll, B., Albert, L., Jayawardhana, R., et al. 2015, *ApJ*, **802**, 28
- Crossfield, I. J. M., Barman, T., Hansen, B. M. S., Tanaka, I., & Kodama, T. 2012, *ApJ*, **760**, 140
- Csizmadia, S., Hellard, H., & Smith, A. M. S. 2019, *A&A*, **623**, A45
- Deming, D., Knutson, H., Kammer, J., et al. 2015, *ApJ*, **805**, 132
- Eastman, J., Gaudi, B. S., & Agol, E. 2013, *PASP*, **125**, 83
- Essick, R., & Weinberg, N. N. 2015, *ApJ*, **816**, 18
- Föhring, D., Dhillon, V. S., Madhusudhan, N., et al. 2013, *MNRAS*, **435**, 2268
- Foreman-Mackey, D., Hogg, D. W., Lang, D., & Goodman, J. 2013, *PASP*, **125**, 306
- Fossati, L., Haswell, C. A., Froning, C. S., et al. 2010, *ApJL*, **714**, L222
- Fulton, B. J., Petigura, E. A., Blunt, S., & Sinukoff, E. 2018, *PASP*, **130**, 044504
- Gelman, A., & Rubin, D. B. 1992, *StaSc*, **7**, 457
- Geweke, J. 1992, *StaSc*, **7**, 94
- Giménez, A., & Bastero, M. 1995, *Ap&SS*, **226**, 99
- Goldreich, P., & Soter, S. 1966, *Icar*, **5**, 375
- Goodman, J., & Weare, J. 2010, *Commun. Appl. Math. Comput. Sci.*, **5**, 65
- Hamer, J. H., & Schlaufman, K. C. 2019, *AJ*, **158**, 190
- Haswell, C. A. 2018, in *Handbook of Exoplanets*, ed. H. J. Deeg & J. A. Belmonte (Cham: Springer International), 97
- Haswell, C. A., Fossati, L., Ayres, T., et al. 2012, *ApJ*, **760**, 79
- Hebb, L., Collier-Cameron, A., Loeillet, B., et al. 2009, *ApJ*, **693**, 1920
- Holman, M., Touma, J., & Tremaine, S. 1997, *Natur*, **386**, 254
- Hooton, M. J., de Mooij, E. J. W., Watson, C. A., et al. 2019, *MNRAS*, **486**, 2397
- Howard, A. W., Johnson, J. A., Marcy, G. W., et al. 2010, *ApJ*, **721**, 1467
- Huang, C., Wu, Y., & Triaud, A. H. M. J. 2016, *ApJ*, **825**, 98
- Husnoo, N., Pont, F., Hébrard, G., et al. 2011, *MNRAS*, **413**, 2500
- Husnoo, N., Pont, F., Mazeh, T., et al. 2012, *MNRAS*, **422**, 3151
- Hut, P. 1980, *A&A*, **92**, 167
- Innanen, K. A., Zheng, J. Q., Mikkola, S., & Valtonen, M. J. 1997, *AJ*, **113**, 1915
- Jackson, B., Arras, P., Penev, K., Peacock, S., & Marchant, P. 2017, *ApJ*, **835**, 145
- Jackson, B., Greenberg, R., & Barnes, R. 2008, *ApJ*, **678**, 1396
- Jackson, B., Jensen, E., Peacock, S., Arras, P., & Penev, K. 2016, *CeMDA*, **126**, 227
- Jia, S., & Spruit, H. C. 2017, *MNRAS*, **465**, 149
- Jones, E., Oliphant, T., Peterson, P., et al. 2001, SciPy: Open source scientific tools for Python, <http://www.scipy.org/>
- Jordán, A., & Bakos, G. A. 2008, *ApJ*, **685**, 543
- Knutson, H. A., Fulton, B. J., Montet, B. T., et al. 2014, *ApJ*, **785**, 126
- Kreidberg, L. 2015, *PASP*, **127**, 1161
- Kreidberg, L., Line, M. R., Bean, J. L., et al. 2015, *ApJ*, **814**, 66
- Lai, D., Helling, C., & van den Heuvel, E. P. J. 2010, *ApJ*, **721**, 923
- Levrard, B., Winisdoerffer, C., & Chabrier, G. 2009, *ApJL*, **692**, L9
- Li, S.-L., Miller, N., Lin, D. N. C., & Fortney, J. J. 2010, *Natur*, **463**, 1054
- Luger, R., Agol, E., Kruse, E., et al. 2016, *AJ*, **152**, 100
- Maciejewski, G., Dimitrov, D., Fernández, M., et al. 2016, *A&A*, **588**, L6
- Maciejewski, G., Dimitrov, D., Seeliger, M., et al. 2013, *A&A*, **551**, A108
- Maciejewski, G., Errmann, R., Raetz, S., et al. 2011, *A&A*, **528**, A65
- Maciejewski, G., Fernández, M., Aceituno, F., et al. 2018, *AcA*, **68**, 371
- Mandel, K., & Agol, E. 2002, *ApJL*, **580**, L171
- Mazeh, T., Krymowski, Y., & Rosenfeld, G. 1997, *ApJL*, **477**, L103
- Meibom, S., & Mathieu, R. D. 2005, *ApJ*, **620**, 970
- Millholland, S., & Laughlin, G. 2018, *ApJL*, **869**, L15
- Miralda-Escudé, J. 2002, *ApJ*, **564**, 1019
- Nichols, J. D., Wynn, G. A., Goad, M., et al. 2015, *ApJ*, **803**, 9
- Ogilvie, G. I. 2014, *ARA&A*, **52**, 171
- Öztürk, O., & Erdem, A. 2019, *MNRAS*, **486**, 2290
- Pál, A., & Kocsis, B. 2008, *MNRAS*, **389**, 191
- Patra, K. C., Winn, J. N., Holman, M. J., et al. 2017, *AJ*, **154**, 4
- Patra, K. C., Winn, J. N., Holman, M. J., et al. 2019, submitted
- Penev, K., Bouma, L. G., Winn, J. N., & Hartman, J. D. 2018, *AJ*, **155**, 165
- Penev, K., Jackson, B., Spada, F., & Thom, N. 2012, *ApJ*, **751**, 96
- Petrucchi, R., Jofré, E., Gómez Maqueo Chew, Y., et al. 2019, *MNRAS*, **491**, 1243
- Ragozzine, D., & Wolf, A. S. 2009, *ApJ*, **698**, 1778
- Rappaport, S., Sanchis-Ojeda, R., Rogers, L. A., Levine, A., & Winn, J. N. 2013, *ApJL*, **773**, L15
- Rasio, F. A., Tout, C. A., Lubow, S. H., & Livio, M. 1996, *ApJ*, **470**, 1187
- Ricker, G. R., Winn, J. N., Vanderspek, R., et al. 2014, *Proc. SPIE*, **9143**, 914320
- Sada, P. V., Deming, D., Jennings, D. E., et al. 2012, *PASP*, **124**, 212
- Sasselov, D. D. 2003, *ApJ*, **596**, 1327
- Schwarz, G. 1978, *AnSta*, **6**, 461
- Stefansson, G., Mahadevan, S., Hebb, L., et al. 2017, *ApJ*, **848**, 9
- Steffen, J. H., Ragozzine, D., Fabrycky, D. C., et al. 2012, *PNAS*, **109**, 7982
- Stevenson, K. B., Bean, J. L., Seifahrt, A., et al. 2014, *AJ*, **147**, 161
- Tinyanont, S., Millar-Blanchaer, M. A., Nilsson, R., et al. 2019, *PASP*, **131**, 025001
- Valsecchi, F., Rappaport, S., Rasio, F. A., Marchant, P., & Rogers, L. A. 2015, *ApJ*, **813**, 101
- Valsecchi, F., & Rasio, F. A. 2014, *ApJL*, **787**, L9
- Van Der Walt, S., Colbert, S. C., & Varoquaux, G. 2011, *CSE*, **13**, 22
- Vissapragada, S., Jontof-Hutter, D., Shporer, A., et al. 2019, arXiv:1907.04445
- Vogt, S. S., Allen, S. L., Bigelow, B. C., et al. 1994, *Proc. SPIE*, **2198**, 362
- von Essen, C., Stefansson, G., Mallonn, M., et al. 2019, *A&A*, **628**, A115
- Weinberg, N. N., Sun, M., Arras, P., & Essick, R. 2017, *ApJL*, **849**, L11
- Wilson, J. C., Eikenberry, S. S., Henderson, C. P., et al. 2003, *Proc. SPIE*, **4841**, 451
- Winn, J. N. 2010, in *Exoplanets*, ed. S. Seager (Tucson, AZ: Univ. Arizona Press), 55